

Optimizing searches for electromagnetic counterparts of gravitational wave triggers

MICHAEL W. COUGHLIN,¹ DUO TAO,² MAN LEONG CHAN,³ DEEP CHATTERJEE,⁴ NELSON CHRISTENSEN,^{2,5} SHAON GHOSH,⁴
GIUSEPPE GRECO,^{6,7} YIMING HU,⁸ SHASVATH KAPADIA,⁴ JAVED RANA,⁹ OM SHARAN SALAFIA,¹⁰ AND
CHRISTOPHER STUBBS¹¹

¹*Division of Physics, Math, and Astronomy, California Institute of Technology, Pasadena, CA 91125, USA*

²*Carleton College, Northfield, MN 55057, USA*

³*University of Glasgow, Glasgow G12 8QQ, United Kingdom*

⁴*University of Wisconsin-Milwaukee, Milwaukee, WI 53201, USA*

⁵*Artemis, Université Côte d'Azur, Observatoire Côte d'Azur, CNRS, CS 34229, F-06304 Nice Cedex 4, France*

⁶*INFN, Sezione di Firenze, I-50019 Sesto Fiorentino, Firenze, Italy*

⁷*Università degli Studi di Urbino 'Carlo Bo,' I-61029 Urbino, Italy*

⁸*TianQin Research Center for Gravitational Physics, Sun Yat-sen University, Tangjiawan, Zhuhai 519082, Guangdong, P. R. China*

⁹*Inter-University Centre for Astronomy and Astrophysics, Pune 411007, India*

¹⁰*INAF - Osservatorio Astronomico di Brera Merate, via E. Bianchi 46, I23807 Merate, Italy*

¹¹*Department of Physics, Harvard University, Cambridge, MA 02138, USA*

Department of Astronomy, Harvard University, Cambridge MA 02138, USA

ABSTRACT

With the detection of a binary neutron star system and its corresponding electromagnetic counterparts, a new window of transient astronomy has opened. Due to the size of the error regions, which can span hundreds to thousands of square degrees, there are significant benefits to optimizing tilings for these large sky areas. The rich science promised by gravitational-wave astronomy has led to the proposal for a variety of tiling and time allocation schemes, and for the first time, we make a systematic comparison of some of these methods. We find that differences of a factor of 2 or more in efficiency are possible, depending on the algorithm employed. For this reason, for future surveys searching for electromagnetic counterparts, care should be taken when selecting tiling, time allocation, and scheduling algorithms to maximize the probability of counterpart detection.

1. INTRODUCTION

The era of multi-messenger gravitational-wave astronomy has arrived with the detection of GW170817 (Abbott et al. 2017a) by Advanced LIGO (Aasi et al. 2015) and Advanced Virgo (Acernese et al. 2015) coincident with the detection of both a short gamma-ray burst (SGRB) (Abbott et al. 2017b; Goldstein et al. 2017; Savchenko et al. 2017) and kilonova detected in coincidence (Coulter et al. 2017; Smartt et al. 2017; Abbott et al. 2017c,d). This work is the culmination of significant effort expended in the search for the electromagnetic counterpart of the gravitational waves found by compact binary black hole systems (Abbott et al. 2016a,b, 2017e).

There has been significant optimism for the potential electromagnetic counterparts for emission from binary neutron star and black hole - neutron star systems across timescales and wavelengths (Nakar 2007; Metzger & Berger 2012). A kilonova, arising from sub-relativistic ejecta, in particular has bolometric luminosities of $\approx 10^{40} - 10^{42}$ ergs/s (Metzger et al. 2015; Barnes

& Kasen 2013) (GW170817 peaked at $\approx 10^{42}$ ergs/s (Smartt et al. 2017)) and color and durations dependent on the physical conditions of the merger (Metzger et al. 2010; Kasen et al. 2013; Barnes & Kasen 2013; Tanaka & Hotokezaka 2013; Kasen et al. 2015; Barnes et al. 2016; Metzger 2017).

The scientific output from a joint gravitational-wave and electromagnetic observation is significant, as the detection of a kilonova coincident with a gravitational wave allows for the exploration of the neutron star equation of state (Bauswein et al. 2013) and r-process nucleosynthesis in the unbound ejecta from a merger involving a neutron star (Metzger et al. 2015; Just et al. 2015; Roberts et al. 2017; Wu et al. 2016). Among others, Smartt et al. (2017) use photometry of GW170817 to place constraints on the ejecta mass, velocity, and effective opacity. Radice et al. (2018) use photometry of GW170817 in conjunction with kilonova models and numerical-relativity results to place a lower bound on the tidal deformability parameter. The identification of the host galaxy allows for a distance-ladder independent measurement of the Hubble Constant (Abbott et

al. 2017f). In addition, the joint observation with a short gamma-ray burst confirms these phenomena are driven by compact binary mergers, but also allow for the study of their beaming, energetics, and galactic environment (Metzger & Berger 2012).

To facilitate the detection of gravitational-wave counterparts, probability skymaps as a function of sky direction and distance are released for gravitational wave triggers produced by the detectors (Singer et al. 2014; Berry et al. 2015). Due to the significant sky coverage required to observe the gravitational-wave sky localization regions, usually spanning $\approx 100 \text{ deg}^2$, techniques to optimize the followup efforts are of significant utility (Fairhurst 2009, 2011; Grover et al. 2014; Wen & Chen 2010; Sidery et al. 2014; Singer et al. 2014; Berry et al. 2015; Essick et al. 2015; Cornish & Littenberg 2015; Klimenko et al. 2016). Given the large sky localization regions involved, wide-field survey telescopes have the best opportunities to make a detection. The Panoramic Survey Telescope and Rapid Response System (Pan-STARRS) (Morgan et al. 2012), Asteroid Terrestrial-impact Last Alert System (ATLAS) (Tonry 2011), the intermediate Palomar Transient Factory (PTF) (Rau et al. 2009) and (what will become) the Zwicky Transient Facility (ZTF), BlackGEM (Bloemen et al. 2015) and the Large Synoptic Survey Telescope (LSST) (Ivezic et al. 2008) are all examples of such systems. For example, Pan-STARRS has a 7 deg^2 field of view (FOV), achieving a 5σ limit of 21.5 (AB mag) in the i band in a 45 second exposure. ATLAS has a 29.2 deg^2 field of view, achieving a 5σ limit of 18.7 in the cyan band in a 30 second exposure. For comparison, LSST will have a 9.6 deg^2 FOV and will require a 21 s r-band exposure length to reach 22 mag.

Due to the significant difference in telescope configurations, including FOV, filter, typical exposure times, and limiting magnitudes, in addition to placement on the earth and therefore different seeing and sky conditions, optimizing gravitational wave followups for generic telescopes is difficult. Therefore, in the following, we will take the telescopes mentioned above as examples.

For this reason, we have created a codebase named *gwemopt* (Gravitational Wave - Electromagnetic OPTimization) that utilizes methods from a variety of recent papers geared towards optimizing efforts of followup. We employ methods to read gravitational-wave skymaps and the associated information made available from GraceDB ¹ (Abbott et al. 2016c), in addition to information about the telescopes to tile the sky, allo-

cate available telescope time to the chosen fields, and schedule that time in a way that optimizes based on expected lightcurves. In section 2, we describe the algorithm. In section 3, we describe the performance of the algorithms. In section 4, we offer concluding remarks and suggest directions for future research.

2. ALGORITHM

Figure 1 shows the flowchart for the *gwemopt* pipeline, developed to optimize the efforts of electromagnetic followup of gravitational-wave events. *gwemopt* is developed in python, which has the benefit of interfaces to both LIGO’s gravitational-wave candidate event database (GraceDB) and HEALPIX (Górski et al. 2005), the format in which LIGO reports skymaps. In the following, we will show the command line syntaxes required to reproduce the results at the beginning of each section.

gwemopt uses events provided by gracedb in addition to information about the telescopes for creating tiles and optimize time allocations in the fields. It uses information about potential lightcurves from electromagnetic counterparts to schedule the available telescope time. In the following, we will describe the calculations that go into creating tiling, time allocations, and observing sequences from the skymaps. We will account for both diurnal and observational constraints and have the possibility of imaging over many nights.

2.1. GraceDB

```
python gwemopt_run --doEvent --do3D --event G268556
```

GraceDB is a service that provides information on candidate gravitational-wave events and the multimessenger followups performed on them. An API is made available that allows for access to this information. *gwemopt* uses this API to access information pertinent for gravitational-wave followups. First of all, it downloads the gravitational-wave skymap for a given event; an example is shown in Figure 2. In addition, information such as the time of the event and the time delay between the time-of-arrival at the detectors is noted.

2.2. Telescope configuration

```
python gwemopt_run --doEvent --do3D --telescope LSST
```

¹ <https://gracedb.ligo.org>

Telescope	Latitude [deg]	Longitude [deg]	Elevation [m]	FOV [deg]	FOV shape	Filter	Exp. time [s]	Lim. Mag.
ATLAS	20.7204	-156.1552	3055.0	5.46	Square	c	30.0	18.7
Pan-STARRS	20.7204	-156.1552	3055.0	1.4	Circle	i	45.0	21.5
BlackGEM	-29.2612	-70.7313	2400.0	2.85	Square	g	300.0	23.0
LSST	-30.1716	-70.8009	2207.0	1.75	Circle	r	30.0	24.4
ZTF	33.3563	-116.8648	1742.0	6.86	Square	r	30.0	20.4

Table 1. Configuration of telescopes.

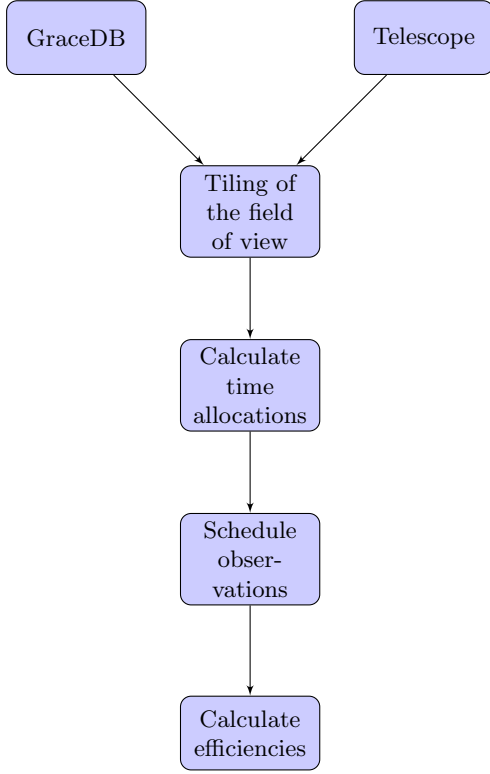


Figure 1. A flow chart of the *gwemopt* pipeline.

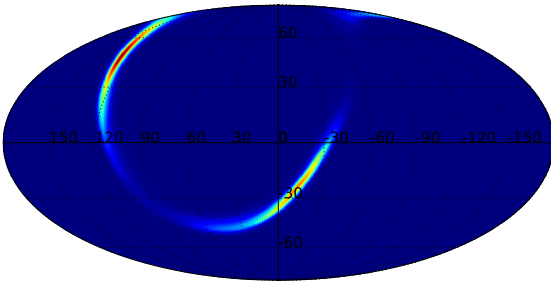


Figure 2. The gravitational-wave likelihood $L_{\text{GW}}(\alpha, \delta, R)$ for GW170104.

gwemopt relies on standardized configuration files for the telescopes to be analyzed (please see ² for examples for the telescopes in Figure 1). The information in these files includes the filter being used, the limiting magnitude of the instrument, the exposure time required to achieve that magnitude, site location information, and information about the field of view shape and size. Different telescopes have different FOV shapes. For this, two options, square and circle are available, with the FOV being specified by the length of the square side and the radius of the circle. In addition, a tessellation-File is requested. This is especially useful for telescopes such as ZTF which use fixed telescope pointings which ensures the availability of reference images. In case a tessellation file is not available, one is automatically generated, and this output is described in the next section. Configuration files for ATLAS, BlackGEM, LSST, PS1, and ZTF are available. Table 1 provides the information assumed for these telescopes.

2.3. Skymap tiling

```
python gwemopt_run --doEvent --do3D --doTiles
                    --doPlots --tilesType ranked
```

Once a telescope configuration has been determined, the next step of the analysis is to generate the sky-map tiling. There are a variety of algorithms in the literature for sky-map tiling, and the ones implemented in *gwemopt* will be detailed below. The idea is to cover the sky with tiles the size of the telescope’s field-of-view with minimal overlap. In some cases, these tiles are pre-determined by survey constraints in order to simplify difference imaging. In other cases, it is possible to optimize the tile locations based on the gravitational-wave skymaps, such that the tiles maximize the probability contained. In the following, we will check the difference between these tile locations to determine their effect. Due to the fields-of-view for these telescopes being in general much smaller than the probability region, the effect is expected to be relatively minimal.

² <https://github.com/mcoughlin/gwemopt/tree/master/config>

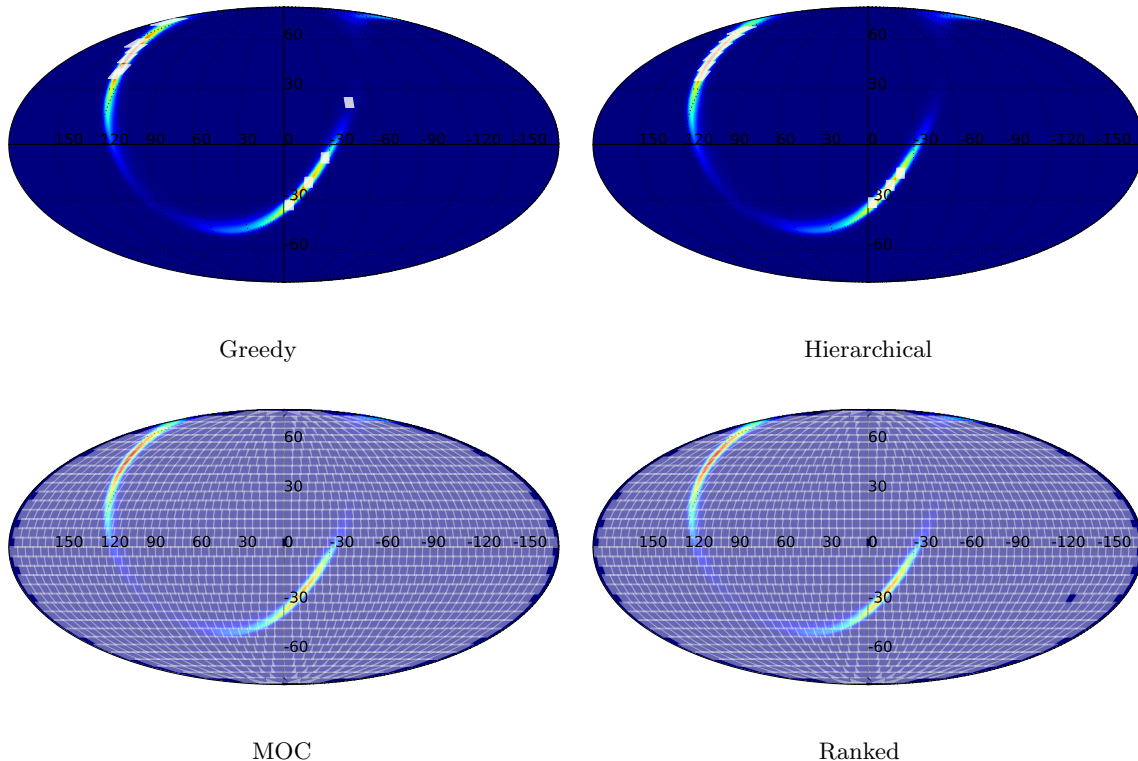


Figure 3. Example outputs of different tiling algorithms. On the top left is the greedy version with $N_{\text{tiles}} = 10$, where N_{tiles} is the number of tiles employed, on the top right is the hierarchical version with the same, on the bottom left is the MOC skymap, and on the bottom right is the ranked skymap tiling.

Gravitational-wave skymaps in general contain metrics that report the spatial probability of a gravitational-wave source lying within a certain location. They are composed of HEALPIX arrays that encode either the 2D probability, in right ascension and declination, or 3D probability, which includes probability distributions for the distance. They are reported in maps with a particular number of pixels, usually $N_{\text{side}} = 512$. This can introduce quantization errors, especially for small field-of-view telescopes. The `-nside` flag allows for the over- or under-sampling of the skymaps in the analysis by up-sampling and down-sampling.

There are four options related to skymap tiling currently available and defined below: MOC, ranked, hierarchical and greedy. In the following, we will summarize the key features of each implementation, and referring the reader to the literature for further details. The goal is to place each algorithm in the same mathematical formalism for straightforward comparisons.

MOC. The “MOC” tiling scheme, based on the multi-order coverage of healpix maps, hierarchically predefines cells in order to specify arbitrary sky regions (Fernique et al. 2014). MOC is proposed in order to provide fast set operations between regions on the sky. In MOC, the spherical sky is recursively divided into 4 regions and

each region is a diamond. The sphere is divided recursively into four diamonds. The division stops according to the resolution necessary for a particular usage. MOC is particularly useful in the case that most information is contained in just a handful of pixels, and therefore it is desired to save that information at high resolution for those pixels, and the remainder of the map at low resolution.

Here are two relevant implementation details about MOC.

- MOC uses an equatorial coordinate system.
- MOC divides the sphere recursively into four diamonds.
- MOC indexes each tile as follows: the initial tile is numbered 0 on level 0. Then, when divided, we get tile indices of 0, 1, 2, 3 on level 1. More generally, if we start from a tile numbered M , its children will be numbered $M \times 4$, $M \times 4 + 1$, $M \times 4 + 2$, $M \times 4 + 3$ on the next level.

ranked. The ranked tiling scheme, described in Ghosh, Shaon et al. (2016), use pre-defined sky cells. This tiling scheme is also based on a grid system with grids of equal sizes such as the one used by MOC. The sizes of the grids

are the same as the size of the telescope FOV. For each tile in the grid at (α_i, δ_i) , we calculate a double integral that accumulates the probability distribution in this tile, shown in Eq.1,

$$T_{ij} = \int_{\alpha_i}^{\alpha_i + \Delta\alpha} \int_{\delta_i}^{\delta_i + \Delta\delta} L_{\text{GW}}(\alpha, \delta) d\Omega \quad (1)$$

where $L_{\text{GW}}(\alpha, \delta)$ is the gravitational-wave likelihood. Then, we rank all the tiles with their T_{ij} and select from the top of the rankings until we reach the target integrated probability desired. In the following, we will take 95% as our target integrated probability, which is a reasonable trade-off between capturing as many potential counterparts as possible while also limiting the sky coverage required.

hierarchical. The hierarchical tiling scheme, which is a Multinest-based (Feroz et al. 2009b,a; Buchner et al. 2014) optimization, chooses tiles for a given skymap by placing them sequentially on the skymap and maximizing the probability at each step. Multinest was chosen because with many nested samples available, the likelihood of the sampler suffering from the natural bimodality of gravitational-wave skymap was lower, as multiple samples could simultaneously explore multiple portions of the skymap at once. We note that any algorithm designed for high-dimensional sampling is possible here. This method starts by selecting the tile that covers the most probability. Then, it sets the probability in that tile to be zero before going to the next iteration, when it again selects the tile that covers the most probability. It stops when a user-specified number of tiles, N_{tiles} , are selected. The tiles selected might overlap on the corners when there are higher probability distributions around that corner.

greedy. The greedy tiling scheme, an emcee (Foreman-Mackey et al. 2013) based algorithm, optimizes tiles for a given skymap by placing them simultaneously. Similar to the Multinest case, any high-dimensional sampler would be reasonable to use here. The algorithm works by taking the user-specified number of tiles, N_{tiles} and allowing their location to vary, with a likelihood that maximizes the integrated probability. It prevents double counting by setting the probability of a given tile to zero when integrating the probability. This method selects tiles that cover the highest probability altogether from the skymap. It ranks all possible tiles and selects from the top. Thus, the tiles selected by greedy method might overlap significantly when the probability distribution is concentrated.

2.4. Time allocations

```
python gwemopt_run --doEvent --doPlots --doTiles
--doSchedule --timeallocationType coverage
```

Once the tile locations have been assigned, whether dynamically or having been fixed previously, the next task is to assign time allocations to each tile, based on a variety of metrics. Because telescopes have fields of view that are in general significantly smaller than the probability region and typical exposure times for these telescopes are of order minutes (see Table 1), it is not possible to image the entire probability region to interesting limiting magnitudes in a reasonable amount of time. There are further constraints that arise from the diurnal cycle, observing time available for followup, limitations on the pointing a particular telescope is capable of, and the rising and setting of tiles. The following algorithms use a variety of methods to optimize the probability of imaging a counterpart with the constraint of limited telescope resources.

The amount of time allocated is defined with a few constraints. First of all, time segments are generated based on the observing time allocated after the gravitational-wave event. In the following analyses, the default will be to assume the following 3 days are available. The segments are then intersected with night time at the site of the particular telescope. This defines the available segments. The time available for the analysis is then determined from these segments. This assumes implicitly that the electromagnetic counterpart has not faded beyond detection limits in the time available. Some of the time allocation algorithms below will use models to determine when the counterpart is expected to be too faint to be detectable.

There are four options related to time allocations as a function of sky location available, powerlaw, WAW (Where and when), PEM (Probability of electromagnetic counterpart), and coverage. Figure 4 shows examples of the powerlaw, WAW, and PEM types.

Coverage. The “coverage” option is one whereby coverage from existing surveys, including the right ascension and declination of the pointing and the limiting magnitude, are used. The benefit of this mode is to establish efficiencies of detection of kilonovae in existing surveys. For example, this code will be used to determine the efficiencies of the Pan-STARRS and ATLAS surveys to both gravitational-wave and gamma-ray burst triggers.

Powerlaw. The “powerlaw” option is one where scaling relations are applied to the probability map to determine the time allocation. Many searches have used a variation on simply scaling the time allocation proportional to the probability skymaps, a technique

employed in the Powerlaw method below. Coughlin & Stubbs (2016) derived scaling relations for the time allocated to any given field, t_i , given the gravitational-wave likelihood. We showed that under certain assumptions, $t_i \propto \left(\frac{L_{GW}(\alpha_i, \delta_i)}{a(\alpha_i, \delta_i)} \right)^{2/3}$, where $L_{GW}(\alpha_i, \delta_i)$ is the gravitational-wave likelihood and $a(\alpha_i, \delta_i)$ is Galactic extinction. While the powerlaw based analysis is straightforward, it does not account for the fact that the telescope must be sensitive enough to detect the counterpart. In this sense, this algorithm is the least model dependent. Although the detectability is model-dependent, both in the distances returned by the gravitational-wave detectors and the absolute magnitude of the sources, the following algorithms account for this in multiple ways.

The *Powerlaw* algorithm optimizes the probability of detecting the transient with N observations, which is simply the sum of the probability of each observation. The expression is shown in Eq. 2:

$$p_{tot} = \sum_{i=1}^N \frac{M_i}{M_{tot}} \frac{L_{GW}(\alpha_i, \delta_i, R_i)}{L_{GW_{tot}}} \frac{F_i(t_i)}{a(\alpha_i, \delta_i)}, \quad (2)$$

where M_i is the mass for galaxy i ; M_{tot} is the total mass of galaxies in the field; $L_{GW}(\alpha_i, \delta_i, R_i)$ is the likelihood of the gravitational wave source in this galaxy; $F(t)$ is the luminosity as a function of allocated time; $a(\alpha_i, \delta_i)$ is the attenuation. In the following, we will simply scale the gravitational-wave likelihood and not the mass in the field. It is possible that this approximation could be improved using galaxy catalogs, although this introduces concerns about galaxy catalog completeness. Eq. 2 is optimized with the constraint that the total observation time is limited, shown as

$$\sum_{i=1}^N t_i = T, \quad (3)$$

where T is the total observation time.

WAW. The “When and Where” algorithm, defined in Salafia et al. (2017), uses counterpart lightcurve models in the optical, infrared and radio constructed from information from the gravitational-wave signals to create a time- and sky location dependent probability for detecting electromagnetic transients. The WAW approach introduces time into the model by defining a concept of detectability. Detectability is the probability of detecting a light flux greater than the flux limit at position α and time t . Thus, by having detectability introduced, the algorithm can optimize “where” and “when” to schedule the observation based on α and t with a greedy approach. The procedures of the algorithm are shown below.

1. The tiles are generated covering the confidence region based on the probability distribution, which comes from the gravitational wave signal.
2. The algorithm takes in the information encoded in the gravitational waves and computes the lightcurve $F_i(t)$ for each tile.
3. Then, it computes the detectability as

$$P(F(t) > F_{lim} | \alpha, S) \approx \sum_{i=1}^N \omega_i H(F_i(t) - F_{lim}) \quad (4)$$

where H is the Heaviside function so if $F_i(t)$ is greater than F_{lim} , it is 1; otherwise it is 0. $F_i(t)$ is the light flux for position sample i at time t . F_{lim} is the limit flux. ω_i is the “inverse distance weight” that gives the contribution of the sample i to position α . The further away sample i is from α , the less it contributes. ω_i is normalized so that $\sum_{i=1}^N \omega_i = 1$.

4. For each tile, we find a time interval $[t_{E,\lambda}, t_{L,\lambda}]$ when the detectability is greater than a threshold λ .
5. We start from the tiles that cover the most probability and arrange their observation times $[t_{E,\lambda}, t_{L,\lambda}]$ if the time is available.

This method optimizes the search by introducing detectability, defined as Eq. 4 over the three dimensional observation volume of direction and time, with the constraint that only one location can be observed at the same time.

PEM. The “Probability of electromagnetic counterpart” algorithm, defined in Chan et al. (2017), optimizes the number of fields to observe and their time allocations by adopting priors on the intrinsic luminosity of the sources and using knowledge of distance to the counterparts provided by the low-latency gravitational-wave searches through BAYESTAR (Singer & Price 2016) or high-latency parameter estimation from LALInference (Veitch et al. 2015) for compact binary coalescence. More concretely, its input is the sky localization map and information about the telescope. It selects the tiles to observe with a greedy algorithm and allocates the observation time for each tile to maximize the probability of detecting the EM counterpart of the GW event.

The procedures of the algorithm are shown below, and further details can be found in Chan et al. (2017).

1. Based on the sky localization map, locate the tiles that cover the region enclosed by the contour of the target confidence level.

2. These N tiles are ranked based on the total probability covered.
3. We optimize the number of tiles selected and then the time allocation for each selected tile. For all k from 1 to n , we do the following:
 - (a) the top k tiles from the rankings are selected.
 - (b) Eq. 5 is the total detection probability of all the tiles and optimized with Lagrange multiplier with the constraint of Eq. 6, which encodes the limited observational time on the telescope:

$$P(D_{EM}|k) = \sum_{i=1}^{k \leq n} P(D_{EM}|\omega_i^{(k)}, \tau_i^{(i)}, I) \quad (5)$$

$$kT_0 + \sum_{i=1}^k \tau_i^{(i)} = T \quad (6)$$
 where ω_i is the probability density; τ_i is the time allocated and I is the parameters of the telescope, T_0 is the time to adjust the telescope before each observation, τ_i is the time allocated to each tile, and T is the total observation time.
 - (c) We keep track of the best k , the tiles and the time allocation.
4. The optimal tiles $\{\omega_i\}$ and their allocated times $\{\tau_i\}$ for $i = 1 \dots k$ are the output.

2.5. Scheduling

```
python gwemopt_run --doEvent --doPlots --doTiles
--doSchedule --scheduleType weighted
```

Once the time allocated to each tile has been set, the next task is to schedule the observations that both best represent the time requested and optimize the times that are chosen in some way. For example, the tiles could be re-imaged at an approximately fixed cadence so as to measure possible lightcurve evolution. Another option is to simply go as deep as possible in one field to ensure detection of a counterpart there. Other optimizations might employ ordering based on airmass, as sources imaged through higher airmass will have lower signal-to-noise ratios.

For each of the algorithms for the scheduling, the time that each tile is available for observation above the altitude limit is computed. Using the set of segments available to the telescope, these tile-specific segments are intersected with these segments to form a set of visibility segments for each tile. This has the benefit of avoiding issues related to simply tracking the rise and set times

of each tile. To account for lunar sky brightness, we use a model from Coughlin et al. (2016). Any tile whose sky brightness is increased by at least 1 mag is excluded.

There are three options related to scheduling observations, greedy, sear, and weighted. *Greedy*. The “greedy” algorithm, which is the simplest version in the codebase, employs a schedule on the basis of probability contained. The idea is that higher ranked tiles are observed before lower ranked tiles based on this ranking scheme. Rana et al. (2017) implemented a greedy algorithm whereby the field with the highest probability region in a given time window is observed. As this analysis did not include the possibility of multiple exposures for each pointing, it is modified in the analysis to include multiple exposures. The algorithm is as follows:

1. Construct a list of the tiles and number of exposures for each tile based on the time allocation algorithm utilized.
2. For each window, find the sky tiles that are in the current window: $T_0 + (j-1)T_{exp}$ and $T_0 + jT_{exp}$
3. Allocate the window to the sky tile with the greatest probability, and increment the number of exposures for that tile down by 1.

sear (Setting Array). The “Setting Array” algorithm, overcomes the shortcoming of the greedy algorithm to include site visibility. This motivates re-ordering the sequence such that as many tiles can be imaged as possible. Rana et al. (2017) also implemented a version whereby the rising and setting of tiles were accounted for. It uses the idea that observes high probability tiles first, subject to the condition that each tile from the observing sequence must be observed before it sets. The concept of imaging windows are used in this algorithm. We call a tile belongs to a window when the end of its observation time is in the window and denote the i th window with W_i . The algorithm uses the recursive relation between the optimal observation arrangement between the first k windows S_k and the first $k+1$ windows S_{k+1} . The details are shown below.

1. Consider the first window W_1 and initialize S_1 to be the tile that has the highest probability for W_1 .
2. Move on to W_2 and find the two tiles c_1 and c_2 that have the greatest probability density.
3. Compare c_1 and c_2 with S_1 and act depending on the following conditions:
 - If both c_1 and c_2 contain greater probability than S_1 , set S_2 to be $\{c_1, c_2\}$.

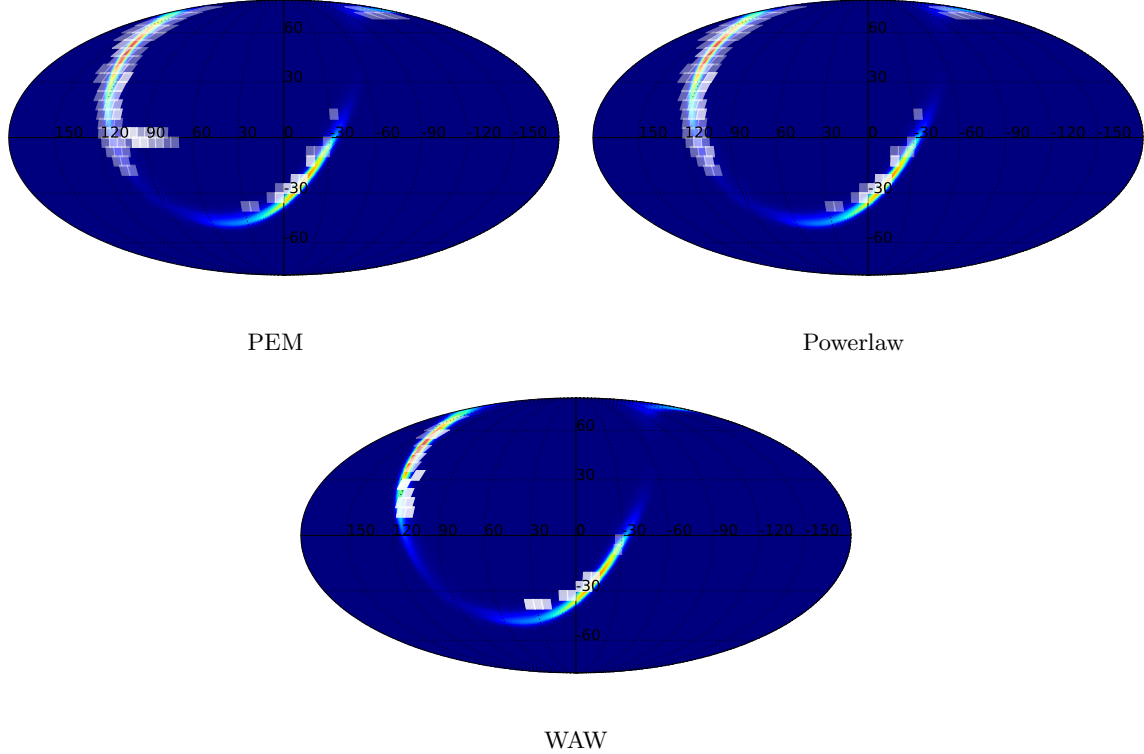


Figure 4. Example outputs of different time allocation algorithms. On the top left is the tiles coverage with the PEM algorithm. On the top right is the tiles coverage with the Powerlaw algorithm. On the bottom is the tiles coverage with the WAW algorithm. In generating all of the plots, MOC algorithm is used.

- Otherwise, put the tile with higher probability coverage between c_1 and c_2 into S_2 , which becomes S_3 .

We can see that either way, S_2 will have two elements.

4. Move on to the next observation windows until the last one. The only difference for the coming iterations from the descriptions above is that S_k will have k elements.
5. Return the last set S_w where w is the total number of observation windows.

weighted. A different scheme, known as “weighted,” is a scheme where each tile is weighted based on both gravitational-wave likelihood enclosed, the number of exposures required for that tile, and the number of available slots for it to be imaged. This is an alternative to the above two, as it is impossible to observe all of the tiles as they rise and set given the requirement of using multiple exposures per tile.

Given the impossibility of necessarily observing all of the tiles as they rise and set is given a weight. Therefore

we define the weights w_i as

$$w_i = L_{\text{GW}}(\alpha_i, \delta_i) \times \frac{N_R}{N_A} \quad (7)$$

Therefore, for each exposure segment, we calculate the weight for each possible tile and select the tile with the highest weight to fill that slot.

2.6. Efficiency

```
python gwemopt_run --doEvent --doPlots --doTiles
                  --doSchedule --doEfficiency
```

We are able to test and compare the performance of these algorithms by performing simulated observations. We adopt observational constraints as follows. We use an observing limit of an altitude of 30° , corresponding to an airmass of 2.0. We assume observations are available to begin at twilight and dawn, corresponding to when the sun is 12° below the western and eastern horizons. We do not point away from the moon or account for sky brightness.

The simplest metric of success is the “efficiency,” which is defined as the number of transients detected over the number of transients injected. To estimate the efficiency for the “detection” of the electromagnetic

counterparts to gravitational-wave transients, we perform simulated injections of supplied lightcurves. We provide example lightcurves for a variety of lightcurve models, including:

1. Tanaka et al. (2014): Simulations of binary systems showing ejecta morphology and resulting lightcurves. These simulations led to analytical models for black-hole neutron star systems from Kawaguchi et al. (2016) and Dietrich & Ujevic (2017).
2. Kawaguchi et al. (2016): Analytical models for black-hole neutron star systems based on Tanaka et al. (2014)
3. Dietrich & Ujevic (2017): Analytical models for binary neutron star systems based on Tanaka et al. (2014)
4. Barnes et al. (2016): Simulations of binary systems studying the emission profiles of radioactive decay products from the merger.
5. Metzger et al. (2015): Blue “precursor” to the kilonovae driven by β -decay of the ejecta mass.
6. Metzger (2017): toy model with grey opacity for lanthanide-free matter with a density profile expanding with a range of velocities with $M(< v) = v^{-1}$.

The requirements for “detection” of the electromagnetic counterparts to gravitational-wave transients are as follows. We require that the transient appear in 2 images over 2 nights. In each image, the transient must exceed the limiting magnitude in that image. The color of the transient is estimated from the filter given in the configuration file. We simulate the transients at a variety of location and distances consistent with the gravitational-wave probability skymap.

3. PERFORMANCE

In this section, we compare the efficiency of the algorithms based on simulated information about what percentage of the events the algorithm can detect. According to the workflow given in Figure 1 and the algorithms given in the sections above, we will have four options for tiling algorithms, three options for time allocation algorithms and another three options for scheduling algorithms. This combines to 36 total options for the whole workflow. We want to know which combination has the best efficiency and then analyze and compare the algorithms individually. We take as an example the ATLAS instrument in the following. As all of the instruments

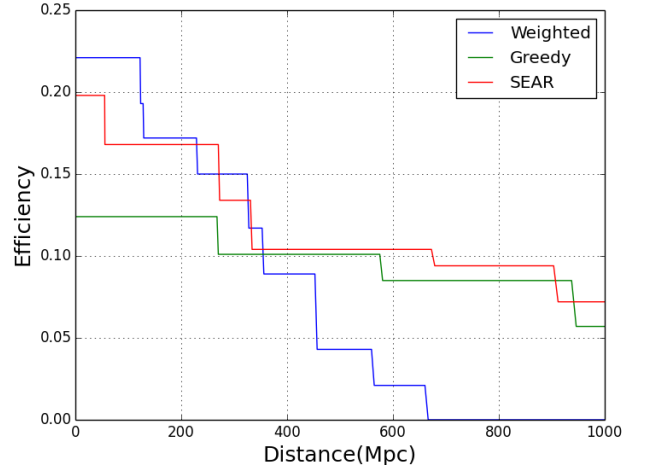


Figure 5. Example plot of efficiency for Metzger (2017) injections, comparing the scheduling algorithms. Greedy algorithm is used for tiling and PEM algorithm is used for time allocation. Greedy and SEAR have similar performance in long distance and both are better than weighted. This difference is also reflected in Figure 6. As the algorithm accounts for observability from a site, including both whether tiles are visible from the site of interest as well as diurnal effects, efficiencies are expected to peak at around 25% for an event which fades quickly and has a probability region with peaks in both the north and south.

are large aperture, wide-field instruments, the results will not strongly depend on the instrument chosen and the way the efficiencies scale will be the same for the level of detail considered here. Including information such as slew and readout time of the individual telescopes will change the results in case of lengthy readout times or characteristically slow slews times.

3.1. Method

We will focus on the model by Metzger (2017) to compare the efficiency. All the efficiency values in the distance range between $10^{-1} Mpc$ to $10^3 Mpc$ (logarithmically spaced) are calculated and plotted. Thus we will have a plot of efficiency against distance for each of the 36 algorithm combinations. An example efficiency plot of efficiency is shown in Figure 5, where difference time allocation algorithms are compared. Greedy algorithm is used for tiling and PEM algorithm is used for time allocation. It can be seen that greedy and sear scheduling does better than weighted at long distance.

In Figure 5, we show an example where we hold the tiling and time allocation algorithms fixed (to disentangle their effects from the scheduling algorithm), and show the efficiency as a function of distance for the scheduling algorithms discussed in this paper. We find that both Greedy and SEAR perform better than

weighted at larger distances. Weighted performs best at the lowest distances considered because it optimizes purely for the highest probability tiles, ensuring that they will be scheduled for multiple exposures so as to meet the detection criteria. Greedy and SEAR, both of which schedule tiles to maximize the number of fields imaged, with SEAR accounting for the rising and setting of the tiles, perform significantly better at greater distances. This is because they sacrifice some efficiency for nearby sources by effectively exploring more fields, but have a more constant detection efficiency with distance.

In order to compare the 36 efficiencies as plotted in Figure 5, we use a single statistic to reflect the overall performance of the algorithms based on the efficiency for each distance in the range of $10^{-1} Mpc$ to $10^3 Mpc$. Thus, we come to a metric that reflects what percentage of events that can be detected in a spherical volume of radius $10^3 Mpc$. The events are evenly distributed in the volume. Suppose the event density per volume is ρ and the distance is r . Sampling a distance at d corresponds to a shell with volume $4\pi r^2 dr$. Assuming that the density is ρ , then the total events on that shell is $4\pi\rho r^2 dr$. Thus, if the efficiency is e , the expected number of detected events on the shell will be $4\pi\rho r^2 e dr$. From this we can see that the efficiency at r is weighted by r^2 . If we treat the efficiency at each distance as an individual sample, a weighted average on the squared radius will then be a good metric of the overall efficiency that reflects how well the algorithm detects events uniformly distributed in a volume of $10^3 Mpc$. A consequence of this metric is that the weight of r^2 makes the long range efficiency more important than short range efficiency. Under this metric, an algorithm that performs well at further distances would be better than an algorithm does better at short distances but whose performance deteriorates quickly as the distance increases.

3.2. Performance and algorithms

For each of the 36 algorithm options, we compute the efficiency metric as described above, which results in 36 numerical efficiency values. The results are plotted in Figure 6. On the horizontal axis are the combined options for the tiling algorithm and scheduling algorithm. There are four tiling algorithms and three scheduling algorithm so they combine to 12 columns on the horizontal axis. Abbreviations are used for the algorithms. The first capital letter stands for the tiling algorithm and the second letter stands for the scheduling algorithm. On the vertical axis are the time allocation algorithms. The color in the 36 boxes shows the efficiency as measured above. The colors are scaled to the efficiency such that higher efficiencies are more darkly colored. The highest

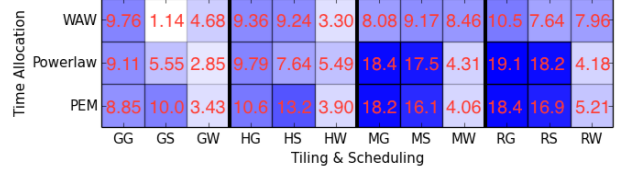


Figure 6. Plot of the efficiency metric for each of the 36 options. On the horizontal axis are tiling algorithms and scheduling algorithms and on the vertical axis are the time allocation algorithms. Abbreviations are used for the algorithms. The first capital letter stands for the tiling algorithm and the second letter stands for the scheduling algorithm. The abbreviations are the first letters of the algorithms: G - greedy. H - hierarchical. M - MOC. R - ranked. S - SEAR. W - weighted. The grids are colors such that highest efficiency combinations are darker and lower efficiency ones are lighter, with the highest being completely blue and the lowest one being completely white.

efficiency of 0.19 is achieved by a combination of ranked tiling, powerlaw time allocation and greedy scheduling. Compared to the lowest efficiency of 0.01, it can detect roughly 19 times more events within a range of $10^{-1} Mpc$ and $10^3 Mpc$. That corresponds to the darkest box in the 10th column and the second row in Figure 6.

Also, from Figure 6, we can compare the efficiencies of the individual algorithms. We concentrate on the SEAR scheduling algorithm in the following, as that was generally seen to be the most efficient from Figure 5. For example, in the case of the use of the MOC tiling algorithm, where all (non-overlapping) tiles are available for allocation, we can look at the “MS” column. The performance of PEM and power-law are very similar, and this fact holds true for all of the configurations. This behavior occurs that despite not using the distance posteriors as PEM does, the powerlaw algorithm encodes the way the likelihood should be allocated with distance in its powerlaw term, and when considering distances where the “shot-noise” of galaxies disappears, they become equivalent. WAW suffers somewhat from the lack of the asset that makes it most valuable: inclusion of the dependence of lightcurves on the inclination angle of the original binary. Therefore, it is not surprising that PEM outperforms WAW in this instance, as PEM is optimal in the presence of distance information, while WAW requires inclination information in order to be optimal. However, in case inclination and distance were available in low latency, WAW may be best. The lower efficiencies in the case of overlapping tiles of the greedy and hierarchical tiling algorithms is due to the upperlimit of on the number of tiles posed (to be returned to in the next section), while performing similarly to one another. This is unsurprising, as both algorithms differ only in the order

in which tiles are determined (greedy optimizes the location all at once, while hierarchical places one tile after the other).

3.3. Performance and the number of tiles

We also study the how the number of tiles affects the performance. It is only relevant in the hierarchical and greedy tiling algorithm. The hierarchical algorithm is used for this study, which selects tiles that covers the highest probability and mask the tiles once they are selected. It stops when a user-defined number of tiles is selected. The efficiency is computed based on the simulation of 1000 injections.

From the plot on the left of Figure 7, it can be seen that considering more tiles generally results in better efficiency. However, the benefit of increasing the number of tiles decreases as more and more tiles are considered. This effect is shown in the left plot, where the efficiency curves are shown for different numbers of tiles. The three lines showing the results of 16, 28 and 40 tiles are closer to each other than the bottom one where only four tiles are selected. This means that increasing the number of tiles from 4 to 16 improves the efficiency more than from 16 to 28. This is expected since, as the number of tiles increases, new tiles cover less and less probability and the limiting factors in the time allocation and scheduling algorithm become more important and the efficiency will not keep rising. Note that the number of tiles in our study is the direct output of the tiling algorithm. A tile still needs to go through the time allocation and scheduling algorithm to be scheduled for observation. It is independent of the CCD readout time and telescope slew. For an alternative study that accounts for these effects, please see [Chan et al. \(2017\)](#).

4. CONCLUSION

The detection of GW170817 ([Abbott et al. 2017a](#)) has invigorated the search for improved strategies for associating gravitational waves with electromagnetic counterparts. Due to the large uncertainty footprint, which can range from 100-1000 square degrees, efficiently scanning sky areas of this size in search of an electromagnetic counterpart is challenging. However, we have described in this paper a number of algorithms in the literature available for significantly improving upon the most naive approach. We have shown comparisons between the algorithms, describing the limits in which they are the most effective.

One potential improvement to the analysis considered here is using the locations of known galaxies in the gravitational-wave sensitivity volume, which was

≈ 100 Mpc for GW170817 ([Abbott et al. 2017a](#)) and will extend to ≈ 300 Mpc at design sensitivity ([Aasi et al 2015](#)). Recent improvements in galaxy catalog completeness have made this effort possible. For example, the Galaxy List for the Advanced Detector Era (GLADE) galaxy catalog is complete (with respect to a Schechter function) out to ≈ 300 Mpc for galaxies brighter than the median Schechter function galaxy luminosity³. The Census of the Local Universe (CLU) catalog ([Cook et al. 2017](#)) is complete to 85% in star-formation and 70% in stellar mass at 200 Mpc. Within these local volumes, the sky area coverage of galaxies is $\approx 1\%$ [Cook et al. \(2017\)](#), bringing the sky areas searched down by a factor of 100, which makes the possibility of targeted galaxy pointing tractable, especially for small field of view telescopes (see [Arcavi et al. \(2017\)](#) for an example).

Unfortunately, it is not immediately clear how to naturally compare or use the power of galaxy catalogs with the techniques presented for wide-field telescopes here. One expects that there will be two regimes where one technique will be optimized over the other. For galaxy targeted searches, nearby sources with small localization volumes are most optimal, as these dedicated searches will be more sensitive to intrinsically fainter sources than the wide-field surveys. On the other hand, wide-field surveys will be more successful across large localization regions where the distance is not necessarily well constrained. As future work, we intend to explore the benefit of combining the power of both techniques. This may be done by modifying the probability map to include the effects of a discrete mass distribution, similar to that proposed by [Arcavi et al. \(2017\)](#) for assigning priorities to individual galaxies. Instead, the probability map will become a sum of the contributions of the galaxies in any given pixel. For nearby events, this map will likely be very pixellated, given the limited number of galaxies that will contribute significantly. For further away events, this map will closely resemble the original probability map.

Also not addressed in this work is how to determine which sources are the best for allocating telescope on. This is less of an issue for the wide-field, all-sky survey instruments, where these observations change the cadence of the survey but are not strictly time lost to the overall endeavor. On the other hand, this is an essential question for target of opportunity observations where the number of sources that can be followed up is often significantly limited. There has been signifi-

³ <http://aquarius.elte.hu/glade/>

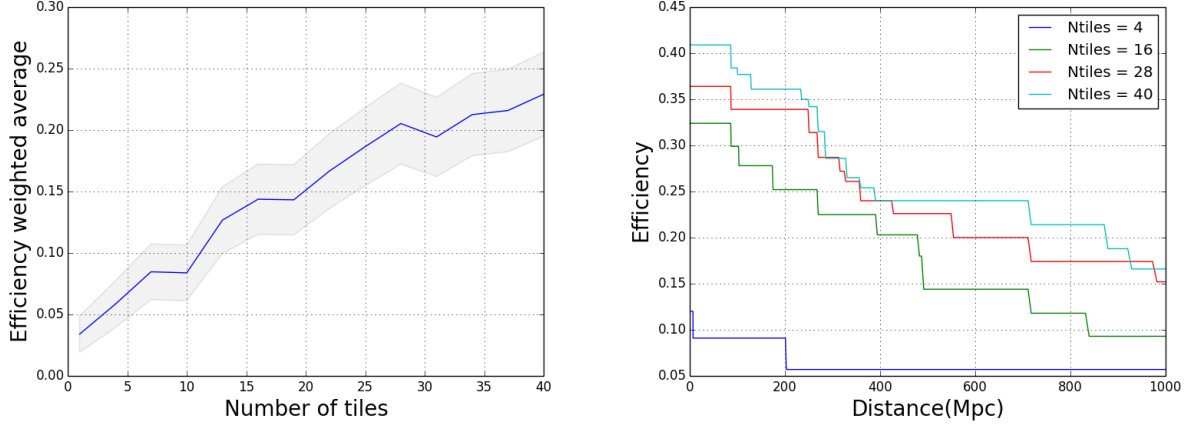


Figure 7. On the left is the plot of efficiency weighted average as a function of the number of tiles considered. On the right is the efficiency curves unpacked from data points corresponding to 4, 16, 28, 40 tiles of the top figure. In the simulation, hierarchical tiling algorithm, power law time allocation algorithm and greedy scheduling algorithm are used to detect 1000 random injections for number of tiles ranging from 1 to 40. The standard deviation is calculated and the 99% confidence interval is plotted as the grey shaded region in the top figure.

cant efforts along these lines recently. For example, ? showed that the localization volume depends strongly on the signal-to-noise ratio of the gravitational-wave event. Therefore, it is likely easier to make a successful observation of the counterpart associated with events with larger signal-to-noise ratio, and therefore it may be best to wait for the loudest events ?. This was also addressed in ?, where it was pointed out that the rate of false positives also significantly increases as a function of signal-to-noise ratio. Going forward, optimizing the choice of events to follow up will be important.

A code to produce the results in this paper is available at <https://github.com/mcoughlin/gwemopt> for public download.

5. ACKNOWLEDGMENTS

MC is supported by the David and Ellen Lee Prize Postdoctoral Fellowship at the California Institute of Technology. DT and NC are supported by the National Science Foundation, under NSF grant number PHY 1505373. YH is supported by the National Natural Science Foundation of China, under NSFC 11703098. CWS is grateful to the DOE Office of Science for their support under award DESC 0007881.

REFERENCES

- Aasi et al. 2015, *Classical and Quantum Gravity*, 32, 074001
- Abbott et al. 2016a, *Phys. Rev. Lett.*, 116, 061102
- . 2016b, *Phys. Rev. Lett.*, 116, 241103
- . 2016c, *Astrophys. J.*, 826, L13
- . 2017a, *Phys. Rev. Lett.*, 119, 161101. <https://link.aps.org/doi/10.1103/PhysRevLett.119.161101>
- . 2017b, *The Astrophysical Journal Letters*, 848, L13. <http://stacks.iop.org/2041-8205/848/i=2/a=L13>
- . 2017c, *The Astrophysical Journal Letters*, 848, L12. <http://stacks.iop.org/2041-8205/848/i=2/a=L12>
- . 2017d, *The Astrophysical Journal Letters*, 850, L39. <http://stacks.iop.org/2041-8205/850/i=2/a=L39>
- . 2017e, *Phys. Rev. Lett.*, 118, 221101
- . 2017f, *Nature*, 551, 85. <http://dx.doi.org/10.1038/nature24471>
- Acernese et al. 2015, *Classical and Quantum Gravity*, 32, 024001
- Arcavi, I., McCully, C., Hosseinzadeh, G., et al. 2017, *The Astrophysical Journal Letters*, 848, L33. <http://stacks.iop.org/2041-8205/848/i=2/a=L33>
- Barnes, J., & Kasen, D. 2013, *Astrophys. J.*, 775, 18
- Barnes, J., Kasen, D., Wu, M.-R., & Martínez-Pinedo, G. 2016, *Astrophys. J.*, 829, 110
- Bauswein, A., Baumgarte, T. W., & Janka, H.-T. 2013, *Phys. Rev. Lett.*, 111, 131101. <https://link.aps.org/doi/10.1103/PhysRevLett.111.131101>
- Berry, C. P. L., Mandel, I., Middleton, H., et al. 2015, *Astrophys. J.*, 804, 114

- Bloemen, S., Groot, P., Nelemans, G., & Klein-Wolt, M. 2015, in *Astronomical Society of the Pacific Conference Series*, Vol. 496, *Living Together: Planets, Host Stars and Binaries*, ed. S. M. Rucinski, G. Torres, & M. Zejda, 254
- Buchner, J., Georgakakis, A., Nandra, K., et al. 2014, *Astron. Astrophys.*, 564, A125
- Chan, M. L., Hu, Y.-M., Messenger, C., Hendry, M., & Heng, I. S. 2017, *The Astrophysical Journal*, 834, 84.
<http://stacks.iop.org/0004-637X/834/i=1/a=84>
- Cook, D. O., Kasliwal, M. M., Van Sistine, A., et al. 2017, *ArXiv e-prints*, arXiv:1710.05016
- Cornish, N. J., & Littenberg, T. B. 2015, *Classical and Quantum Gravity*, 32, 135012.
<http://stacks.iop.org/0264-9381/32/i=13/a=135012>
- Coughlin, M., & Stubbs, C. 2016, *Experimental Astronomy*, 1. <http://dx.doi.org/10.1007/s10686-016-9503-4>
- Coughlin, M., Stubbs, C., & Claver, C. 2016, *Experimental Astronomy*, 41, 393.
<https://doi.org/10.1007/s10686-016-9494-1>
- Coulter et al. 2017, *Science*, 358, 1556
- Dietrich, T., & Ujevic, M. 2017, *Class. Quant. Grav.*, 34, 105014
- Essick, R., Vitale, S., Katsavounidis, E., Vedovato, G., & Klimentko, S. 2015, *The Astrophysical Journal*, 800, 81.
<http://stacks.iop.org/0004-637X/800/i=2/a=81>
- Fairhurst, S. 2009, *New J. Phys.*, 11, 123006
- Fairhurst, S. 2011, *Class. Quant. Grav.*, 28, 105021
- Fernique, P., Boch, T., Donaldson, T., et al. 2014, *MOC - HEALPix Multi-Order Coverage map Version 1.0*, IVOA Recommendation 02 June 2014, , , arXiv:1505.02937
- Feroz, F., Gair, J. R., Hobson, M. P., & Porter, E. K. 2009a, *Class. Quant. Grav.*, 26, 215003
- Feroz, F., Hobson, M. P., & Bridges, M. 2009b, *Mon. Not. Roy. Astron. Soc.*, 398, 1601
- Foreman-Mackey, D., Hogg, D. W., Lang, D., & Goodman, J. 2013, *Publications of the Astronomical Society of the Pacific*, 125, 306.
<http://stacks.iop.org/1538-3873/125/i=925/a=306>
- Ghosh, Shaon, Bloemen, Steven, Nelemans, Gijs, Groot, Paul J., & Price, Larry R. 2016, *Astronomy and Astrophysics*, 592, A82.
<https://doi.org/10.1051/0004-6361/201527712>
- Goldstein et al. 2017, *The Astrophysical Journal Letters*, 848, L14.
<http://stacks.iop.org/2041-8205/848/i=2/a=L14>
- Górski, K. M., Hivon, E., Banday, A. J., et al. 2005, *ApJ*, 622, 759
- Grover, K., Fairhurst, S., Farr, B. F., et al. 2014, *Phys. Rev.*, D89, 042004
- Ivezic, Z., Tyson, J. A., Allsman, R., Andrew, J., & Angel, R. 2008, arXiv:0805.2366
- Just, O., Bauswein, A., Pulpillo, R. A., Goriely, S., & Janka, H.-T. 2015, *Monthly Notices of the Royal Astronomical Society*, 448, 541.
[+http://dx.doi.org/10.1093/mnras/stv009](http://dx.doi.org/10.1093/mnras/stv009)
- Kasen, D., Badnell, N. R., & Barnes, J. 2013, *Astrophys. J.*, 774, 25
- Kasen, D., Fernandez, R., & Metzger, B. 2015, *Mon. Not. Roy. Astron. Soc.*, 450, 1777
- Kawaguchi, K., Kyutoku, K., Shibata, M., & Tanaka, M. 2016, *Astrophys. J.*, 825, 52
- Klimentko, S., Vedovato, G., Drago, M., et al. 2016, *Phys. Rev. D*, 93, 042004.
<http://link.aps.org/doi/10.1103/PhysRevD.93.042004>
- Metzger, B. D. 2017, *Living Rev. Rel.*, 20, 3
- Metzger, B. D., Bauswein, A., Goriely, S., & Kasen, D. 2015, *Mon. Not. Roy. Astron. Soc.*, 446, 1115
- Metzger, B. D., & Berger, E. 2012, *Astrophys. J.*, 746, 48
- Metzger, B. D., Martínez-Pinedo, G., Darbha, S., et al. 2010, *Monthly Notices of the Royal Astronomical Society*, 406, 2650
- Morgan, J. S., Kaiser, N., Moreau, V., Anderson, D., & Burgett, W. 2012, *Proc. SPIE Int. Soc. Opt. Eng.*, 8444, 0H
- Nakar, E. 2007, *Phys. Rept.*, 442, 166
- Radice et al. 2018, *The Astrophysical Journal Letters*, 852, L29. <http://stacks.iop.org/2041-8205/852/i=2/a=L29>
- Rana, J., Singhal, A., Gadre, B., Bhalariao, V., & Bose, S. 2017, *The Astrophysical Journal*, 838, 108.
<http://stacks.iop.org/0004-637X/838/i=2/a=108>
- Rau, A., Kulkarni, S. R., Law, N. M., et al. 2009, *Publ. Astron. Soc. Pac.*, 121, 1334
- Roberts, L. F., Lippuner, J., Duez, M. D., et al. 2017, *Monthly Notices of the Royal Astronomical Society*, 464, 3907. [+http://dx.doi.org/10.1093/mnras/stw2622](http://dx.doi.org/10.1093/mnras/stw2622)
- Salafia, O. S., Colpi, M., Branchesi, M., et al. 2017, *The Astrophysical Journal*, 846, 62.
<http://stacks.iop.org/0004-637X/846/i=1/a=62>
- Savchenko, V., Ferrigno, C., Kuulkers, E., et al. 2017, *The Astrophysical Journal Letters*, 848, L15.
<http://stacks.iop.org/2041-8205/848/i=2/a=L15>
- Sidery, T., Aylott, B., Christensen, N., et al. 2014, *Phys. Rev.*, D89, 084060
- Singer, L. P., & Price, L. R. 2016, *Phys. Rev. D*, 93, 024013.
<https://link.aps.org/doi/10.1103/PhysRevD.93.024013>
- Singer, L. P., Price, L. R., Farr, B., et al. 2014, *Astrophys. J.*, 795, 105
- Smartt et al. 2017, *Nature*, 551, 75 EP .
<http://dx.doi.org/10.1038/nature24303>

- Tanaka, M., & Hotokezaka, K. 2013, *Astrophys. J.*, 775, 113
- Tanaka, M., Hotokezaka, K., Kyutoku, K., et al. 2014, *Astrophys. J.*, 780, 31
- Tonry, J. L. 2011, *Publ. Astron. Soc. Pac.*, 123, 58
- Veitch, J., Raymond, V., Farr, B., et al. 2015, *Phys. Rev. D*, 91, 042003.
<https://link.aps.org/doi/10.1103/PhysRevD.91.042003>
- Wen, L., & Chen, Y. 2010, *Phys. Rev.*, D81, 082001
- Wu, M.-R., Fernández, R., Martinez-Pinedo, G., & Metzger, B. D. 2016, *Monthly Notices of the Royal Astronomical Society*, 463, 2323.
[+http://dx.doi.org/10.1093/mnras/stw2156](http://dx.doi.org/10.1093/mnras/stw2156)